NOAA Technical Memorandum ERL WPL-93

RADAR GEOMETRY OF SURFACE VELOCITY MAPS

James A. Leise

Wave Propagation Laboratory
Boulder, Colorado
February 1982

noaa NATIONAL OCEANIC AND
ATMOSPHERIC ADMINISTRATION / Environmental Research
Laboratories
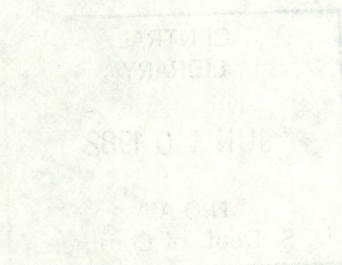
NOAA Technical Memorandum ERL WPL-93

RADAR GEOMETRY OF SURFACE VELOCITY MAPS

James A. Leise

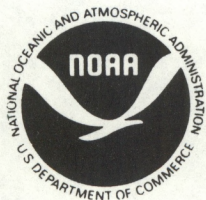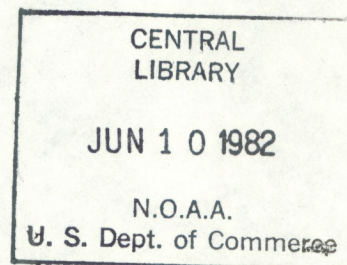Wave Propagation Laboratory
Boulder, Colorado
February 1982

82 01251

CONTENTS

RADAR GEOMETRY OF SURFACE VELOCITY MAPS

James A. Leise

ABSTRACT

A single radar measures one degree of freedom, the radial velocity component; the natural geometry is polar-coordinate. Polar data from two radars can, in turn, be combined to resolve two-dimensional Cartesian vectors. The transformation that does this conversion is derived; instabilities are studied; error curves are given; ground-truth experimental design is discussed. In particular, a method for extending over instabilities is presented.

I.   INTRODUCTION

The geometric transformation of two polar-coordinate systems to a rectangular one is a basic mathematical procedure that has been analyzed by Miller and Strauch [1]. Their approach was largely statistical; ours is geometric. Mathematically, the geometric approach is more direct and penetrating; instabilities are more easily visualized and studied.

The geometric transformation has two instabilities. The first results from an inability to resolve more than one degree of freedom along the baseline connecting the two sites; the second results from an inability to resolve more than one degree of freedom at great distances. The first instability is called *baseline instability*; we call the second *outer instability*. Of the two, baseline instability is usually the more troublesome because it occurs close to the radars where the signal-to-noise ratio (SNR) of the polar velocity data is best.

Effective control of these instabilities is realized with a moving coordinate system which we call *triangulation-coordinates*; it depends on the triangulation of a point with the two radar sites. It is an orthogonal system with one stable

(error reducing) and one unstable (error increasing) component; the precision of the stable component increases as the precision of the unstable component decreases.

At some point, errors will dominate the unstable component rendering it useless; at the same time, the quality of the stable component is very good. To avoid wasting good information, we present a *singular extension method* whereby unstable components are deleted and replaced with stable numerical estimates.

Finally, these methods are tested on simulated radial velocity data (filtered and unfiltered). Results show that singular extension is an effective, stable procedure and that low-pass filters applied to one-site polar data tend to suppress transformation instabilities.

II. THE DIRECT TRANSFORMATION

Given two radar sites, there is a natural computational coordinate system in which the baseline connecting the two sites is the x-axis, and the origin is halfway between. Thus, if one site is located at x-distance d, the other is at −d. This two-site geometry is shown in Fig. 1. We see a general point $\bar{P} = (x,y)$ in the plane at distances r_1 and r_2 from the sites:

$$r_1 = [(x-d)^2 + y^2]^{1/2}$$

$$r_2 = [(x+d)^2 + y^2]^{1/2} .$$ (2.1)

The unit direction vectors $\bar{e}_1$ and $\bar{e}_2$ pointing from the respective sites to the point $\bar{P}$ then are

$$\bar{e}_1 = [(x-d)\bar{i} + y\bar{j}]/r_1$$

$$\bar{e}_2 = [(x+d)\bar{i} + y\bar{j}]/r_2 .$$ (2.2)

Now, a single radar can measure only the radial part of the total velocity $\bar{v}$ coming toward or going away from the site. Mathematically, the radial components V_1 and V_2 are the orthogonal projections (dot products) in the directions $\bar{e}_1$ and $\bar{e}_2$:

$$V_1 = \bar{v} \cdot \bar{e}_1 = [(x-d)u + yv]/r_1$$

$$V_2 = \bar{v} \cdot \bar{e}_2 = [(x+d)u + yv]/r_2 \; . \tag{2.3}$$

It is a system of two equations (with data V_1 and V_2) in the two unknowns u and v. Solving gives

$$u = \frac{r_2 V_2 - r_1 V_1}{2d}$$

$$v = \frac{r_1 V_1 (x+d) - r_2 V_2 (x-d)}{2yd} \; . \tag{2.4}$$

This is the direct transformation needed to convert two-site radial data (V_1, V_2) into the Cartesian vector (u,v). It should be noted that as y becomes small or x becomes large, the calculation of v becomes unstable; these instabilities are a form of baseline and outer instability respectively.

III. TRIANGULATION COORDINATES

Instabilities in the polar-coordinate to Cartesian transformation can be traced to the way that radial lines intersect. In Fig. 1, the interior angle of the triangulation is denoted by γ. The line that bisects this angle is one axis of the triangulation-coordinate system; the other axis bisects the complementary angle. Because these bisectors are perpendicular, they define a system of ortho-gonal frames, a system with components analogous to the tangential and radial components of polar-coordinates.

Mathematically, the direction vectors defining triangulation-coordinates are

$$\bar{e}_- = \frac{\bar{e}_2 - \bar{e}_1}{2|\sin(\gamma/2)|}$$

$$(3.1)$$

$$\bar{e}_+ = \sigma \frac{\bar{e}_2 + \bar{e}_1}{2|\cos(\gamma/2)|} \quad , \qquad \sigma = \text{sign}(y) = \pm 1 \quad .$$

A straightforward computation verifies that $\bar{e}_-$ and $\bar{e}_+$ have unit length

$$\bar{e}_- \cdot \bar{e}_- = \bar{e}_+ \cdot \bar{e}_+ = 1 \quad .$$

$$(3.2)$$

Also, they are orthogonal:

$$\bar{e}_- \cdot \bar{e}_+ = 0 \quad .$$

$$(3.3)$$

The interesting feature is that both $\bar{e}_-$ and $\bar{e}_+$ become singular on the x-axis; $\bar{e}_-$ has a zero denominator when $\gamma = 0$; $\bar{e}_+$ has a zero denominator when $\gamma = \pi$. The discontinuity in $\bar{e}_-$ is removable (limits exist); however, the discontinuity in $\bar{e}_+$ is not. The best we can do is move the essential discontinuity into a region where it is least damaging. The choice of $\sigma = \text{sign}(y)$ in (3.1) fixes the essential discontinuity to two branch cuts radiating outward from the sites as shown in Fig. 2. Also shown are the general orientations of $\bar{e}_-$ and $\bar{e}_+$ in the four quadrants. Note that as the x-axis *in between* sites is crossed, the orientation of $\bar{e}_+$ remains upward, and the discontinuity is removable.

In summary, we have shown that the components $\bar{e}_-$ and $\bar{e}_+$ defining triangulation-coordinates are orthogonal unit vectors and are continuous except for two branch cuts which are unobtrusive to most radar processing.

IV. TRIANGULATION ERRORS

A vector velocity $\bar{v}$ can now be expressed in triangulation-coordinates as

$$\bar{v} = V_- \bar{e}_- + V_+ \bar{e}_+$$

$$(4.1)$$

where

$$V_- = \bar{v} \cdot \bar{e}_- = \frac{V_2 - V_1}{2|\sin(\gamma/2)|}$$

(4.2)

$$V_+ = \bar{v} \cdot \bar{e}_+ = \sigma \frac{V_2 + V_1}{2|\cos(\gamma/2)|} \quad .$$

The unstable component is that component V_- or V_+ which has the smallest denominator; it is the component that bisects the larger angle. More precisely, the unstable component is

$$\text{u.c.} = \begin{cases} V_- & , \quad \gamma < \pi/2 \\ \\ V_+ & , \quad \gamma > \pi/2 \quad . \end{cases}$$

(4.3)

Strictly speaking, there is no unstable (or stable) component when $\gamma = \pi/2$; the locus of all such points is a circle of radius d passing through the two sites; inside the circle, V_+ is unstable; outside the circle, V_- is unstable.

Relative errors are obtained by comparing with an error level ε on the circle

$$\text{Error}(\gamma) = \begin{cases} \varepsilon/\sqrt{2}|\sin(\gamma/2)| & , \quad \gamma \leq \pi/2 \\ \\ \varepsilon/\sqrt{2}|\cos(\gamma/2)| & , \quad \gamma \geq \pi/2 \quad . \end{cases}$$

(4.4)

Thus, (4.4) is the amount by which errors ε are amplified (in the unstable component) by moving to a point with triangulation angle γ.

Figure 3 shows error curves obtained by incrementing $\cos(\gamma)$ in steps of ± 0.2; in particular, all are curves of constant triangulation angle γ. The inner regions (solid lines) measure baseline instability, and the far regions (segmented lines) measure outer instability.

In conclusion, we see that the ε-circle is quite special; it consists of those points for which the total vector measurement is most accurate. Values or estimates of ε, however, must be obtained from ground-truth experiments, and consequently the circle is of fundamental importance in such experimental design.

5

V. THE ROTATION

It remains to transform (V_-, V_+) into a Cartesian vector (u,v). This final transformation is a rigid rotation (orthogonal matrix) and, consequently, does not amplify errors. Thus, there exist rotation numbers A and B for which

$$A^2 + B^2 = 1$$

$$V_- = \bar{e}_- \cdot \bar{v} = Au + Bv \qquad (5.1)$$

$$V_+ = \bar{e}_+ \cdot \bar{v} = -Bu + Av \quad .$$

Solving for u and v, in turn, gives

$$u = AV_- - BV_+$$

$$\qquad (5.2)$$

$$v = BV_- + AV_+ \quad .$$

To compute A and B, first evaluate $\bar{e}_-$ and $\bar{e}_+$ from the definitions (3.1) and (2.2).

$$\bar{e}_- = \left[\left(\frac{x+d}{r_2} - \frac{x-d}{r_1} \right) \bar{i} + \left(\frac{y}{r_2} - \frac{y}{r_1} \right) \bar{j} \right] \Big/ 2 |\sin(\gamma/2)|$$

$$\qquad (5.3)$$

$$\bar{e}_+ = \sigma \left[\left(\frac{x+d}{r_2} + \frac{x-d}{r_1} \right) \bar{i} + \left(\frac{y}{r_2} + \frac{y}{r_1} \right) \bar{j} \right] \Big/ 2 |\cos(\gamma/2)| \quad .$$

Two solutions then result by comparing (5.3) with (5.1).

$$\text{Solution I:} \quad \begin{cases} A = \left(\dfrac{x+d}{r_2} - \dfrac{x-d}{r_1} \right) \Big/ 2 |\sin(\gamma/2)| \\[2em] B = y \left(\dfrac{1}{r_2} - \dfrac{1}{r_1} \right) \Big/ 2 |\sin(\gamma/2)| \end{cases} \qquad (5.4)$$

$$
\text{Solution II:} \quad
\begin{cases}
A = \sigma y \left(\dfrac{1}{r_2} + \dfrac{1}{r_1} \right) \Big/ 2 \left| \cos(\gamma/2) \right| \\[2ex]
B = -\sigma \left(\dfrac{x+d}{r_2} + \dfrac{x-d}{r_1} \right) \Big/ 2 \left| \cos(\gamma/2) \right| \ .
\end{cases}
\tag{5.5}
$$

Although both solutions (when they exist) are theoretically identical, Solution I is more stable inside the circle while the Solution II is more stable outside. Thus, both are useful for numerical work.

The factorization of the direct transformation (2.4) through triangulation-coordinates is now complete. The triangulation vector (V_-, V_+) is computed from the radial velocity data (V_1, V_2), and rotated into the Cartesian vector (u,v) using (5.2). A and B are computed from the more stable of the two calculations (5.4) or (5.5).

VI.   SINGULAR EXTENSION

Triangulation-coordinates are particularly useful because they provide a decomposition (V_-, V_+) of the radial data into a most stable and a most unstable part; errors in the unstable components increase at the same rate that errors in the stable components decrease. Therefore, the price of editing out or deleting an unstable component is high; the total velocity is no longer defined; the stable component is therefore lost. The net effect is to discard the good component along with the bad.

A practical way of correcting this situation is to replace the unstable components with numerical estimates. This is justifiable because the instabilities can be traced to near-indeterminate (zero/zero) calculations. Because these indeterminacies can be evaluated as limits (except along the branch cuts of Fig. 2), these numerical estimates can be viewed as limit approximations.

The first step in our singular extension method amounts to deleting the unstable parts of V_- and V_+ to obtain partial fields/arrays $\hat{V}_-$ and $\hat{V}_+$. This is accomplished by specifying a triangulation error level $t\epsilon\,(t > 1)$; thus $\hat{V}_-$ is

obtained from V_- by deleting all points outside the segmented $t\epsilon$-curve of Fig. 3; $\hat{V}_+$ is obtained from V_+ by deleting all points inside the solid $t\epsilon$-curve. This is illustrated in the vector maps of Figs. 4 and 5; Fig. 4 shows a constant signal velocity and synthetic data obtained by adding white noise; Fig. 5 shows the result of deleting the unstable regions corresponding to 2.0ϵ, 1.5ϵ, and 1.25ϵ.

It is important to note that this deletion scheme is purely geometric; it is independent of any particular data set. As such, it is not an editing scheme in the usual sense; an editing scheme would compare/check specific values against some quality criterion; points removed would vary from data set to data set.

We next observe that this deletion really works; baseline instability is evident in the synthetic data of Fig. 4 and this instability is effectively removed in the maps of Fig. 5.

The geometric nature of deletion can be viewed as simply changing the data grid. The underlying computation grid in the examples of Figs. 4 and 5 is, actually, rectangular. The maps appear pointed because of range limitations in the radial data. In Fig. 5, the grid has been confined to even smaller, more stable regions. In effect, the points remaining specify a new grid--a stable computation grid.

We now proceed to replace the deleted unstable components with numerical estimates; the partial fields $\hat{V}_-$ and $\hat{V}_+$ are completed using the extension method of Leise [2]. This is an iterative averaging scheme that fills all points missing from a rectangular grid. A simple masking operation is then used to return the rectangular grid to the range-limited (pointed) grid of Fig. 4.

The result of applying this procedure to the maps of Fig. 5 is shown in Fig. 6. The high-frequency texture appearing in the extended regions is due to the stable component remaining after deletion. It should be noted that extended values common to all three maps are remarkably similar. Thus, extended values are relatively insensitive to the area deleted.

In summary, our singular extension method performs as intended; transformation instabilities are effectively controlled; the extensions are reasonable; the stable

components are well utilized. The only restriction is that the rectangular computation grid cannot cross the branch cuts of Fig. 2.

VII. FILTERING AND INSTABILITIES

As a final topic relating to transformation instabilities, we show that low-pass filters applied to radial data help stabilize numerical computation. We argue by way of examples and, consequently, our conclusions are only qualitative. Because of this, we shall omit specific details related to grid densities and filter parameters.

The filter used is due to Leise [2]; it is a multidimensional algorithm which can be adjusted for different scale sizes. We use three different scale adjustments (steps); we refer to the resulting filters as F_1, F_2, and F_3. Here, F_1 passes higher frequencies than F_2, and F_2 passes higher frequencies than F_3; thus, F_3 is the most potent low-pass filter.

Figure 7 shows the result of applying these filters to the noisy *radial* data used to generate the synthetic data map of Fig. 4. Although baseline instability is evident in the filtered maps, it is dramatically reduced in magnitude. We also observe that as the level of filtering is increased, the effect of baseline instability is decreased.

In Fig. 8, we see the combined results of filtering and component extension. In all three maps, an error level of 2ε was used for the deletion (see the upper map in Fig. 5). The radial data are filtered the same way as before (Fig. 7). The net effect of the combined methods is impressive; instabilities are no longer evident; the maps are more coherent. In particular, the map for the F_3 filter is almost indistinguishable from the signal map of Fig. 4.

In conclusion, we have verified the utility of filtering in suppressing instabilities. We have not, however, addressed the problem of optimal use of filtering and/or singular extension. This is because optimal use often depends on the specific application, as well as the specific accuracy/quality of a given data set. Instead, we have presented and analyzed tools that work over a wide variety of conditions; optimal use rests with the user.

9

VIII. REFERENCES

[1] L.J. Miller and R.G. Strauch, A dual Doppler radar method for the determination of wind velocities within precipitating weather systems, <u>Remote Sensing Environ.</u>, <u>3</u>, pp. 219-235, 1974.

[2] J.A. Leise, A multidimensional scale-telescoped filter and data extension package, NOAA Technical Memorandum ERL WPL-82, 1981.
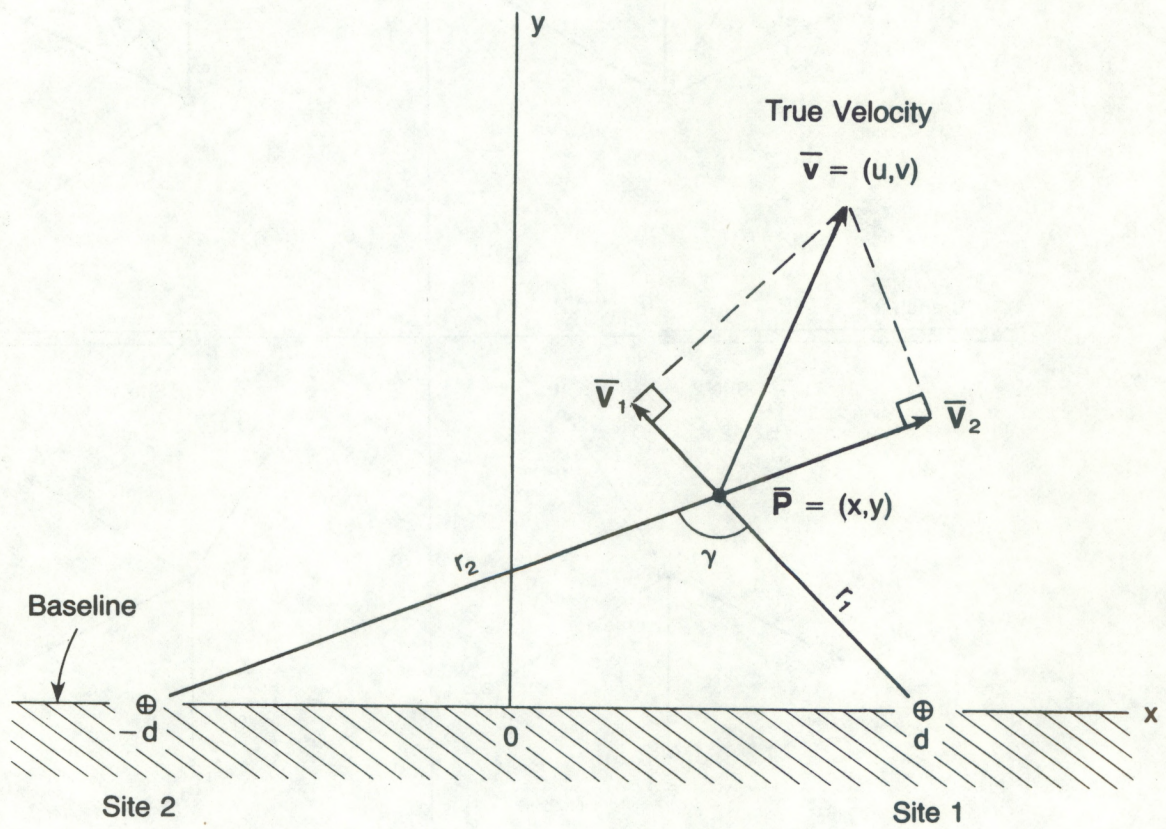
10

Figure 1.—Two-site radar geometry. As the triangulation angle γ is increased, the computation of the total vector velocity $\bar{v}$ from the radial data V_1 and V_2 becomes unstable.

11
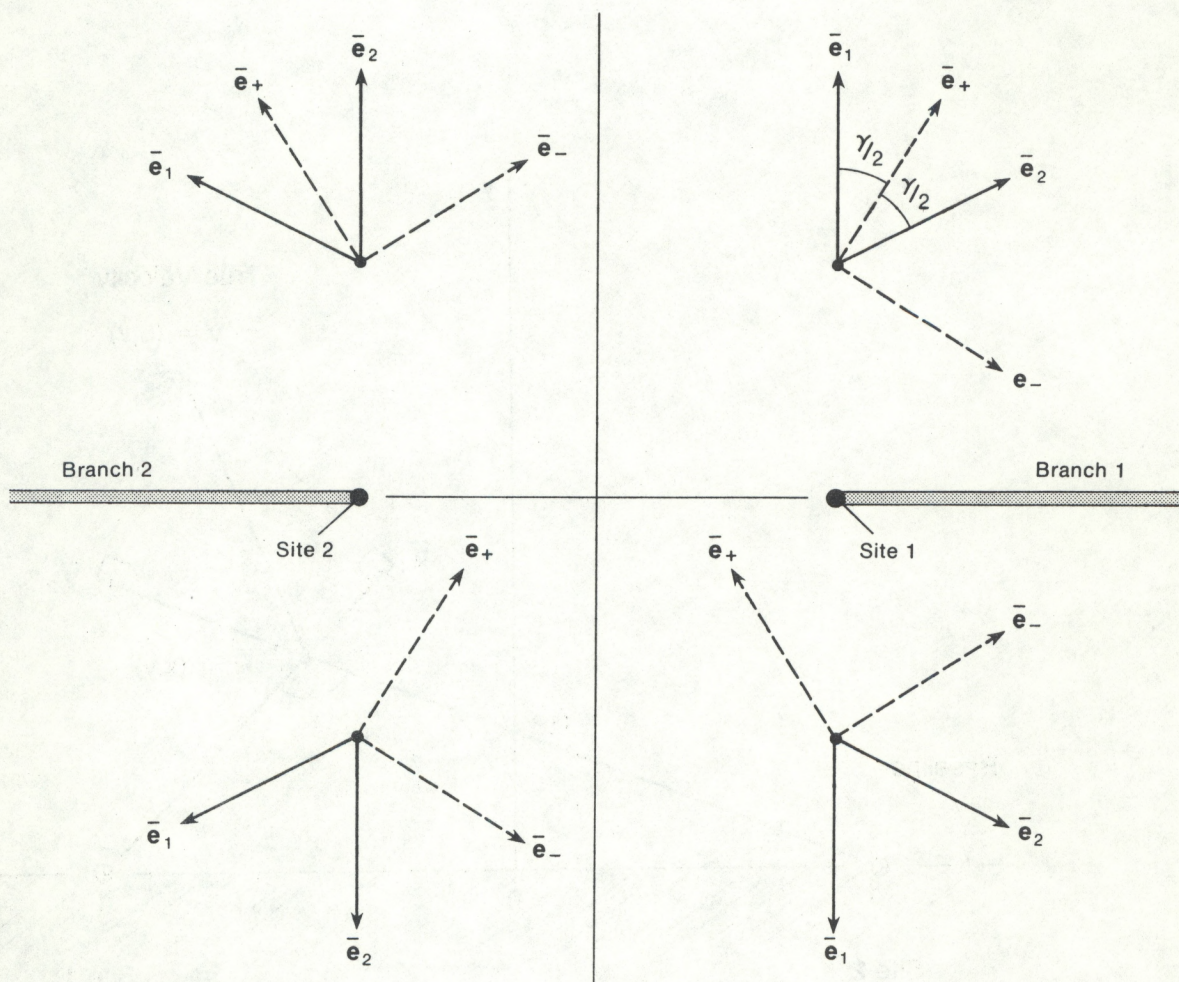
Figure 2.--The direction vectors $\bar{e}_-$ and $\bar{e}_+$ for triangulation coordinates. There is a discontinuity in $\bar{e}_+$ along the branch cuts.
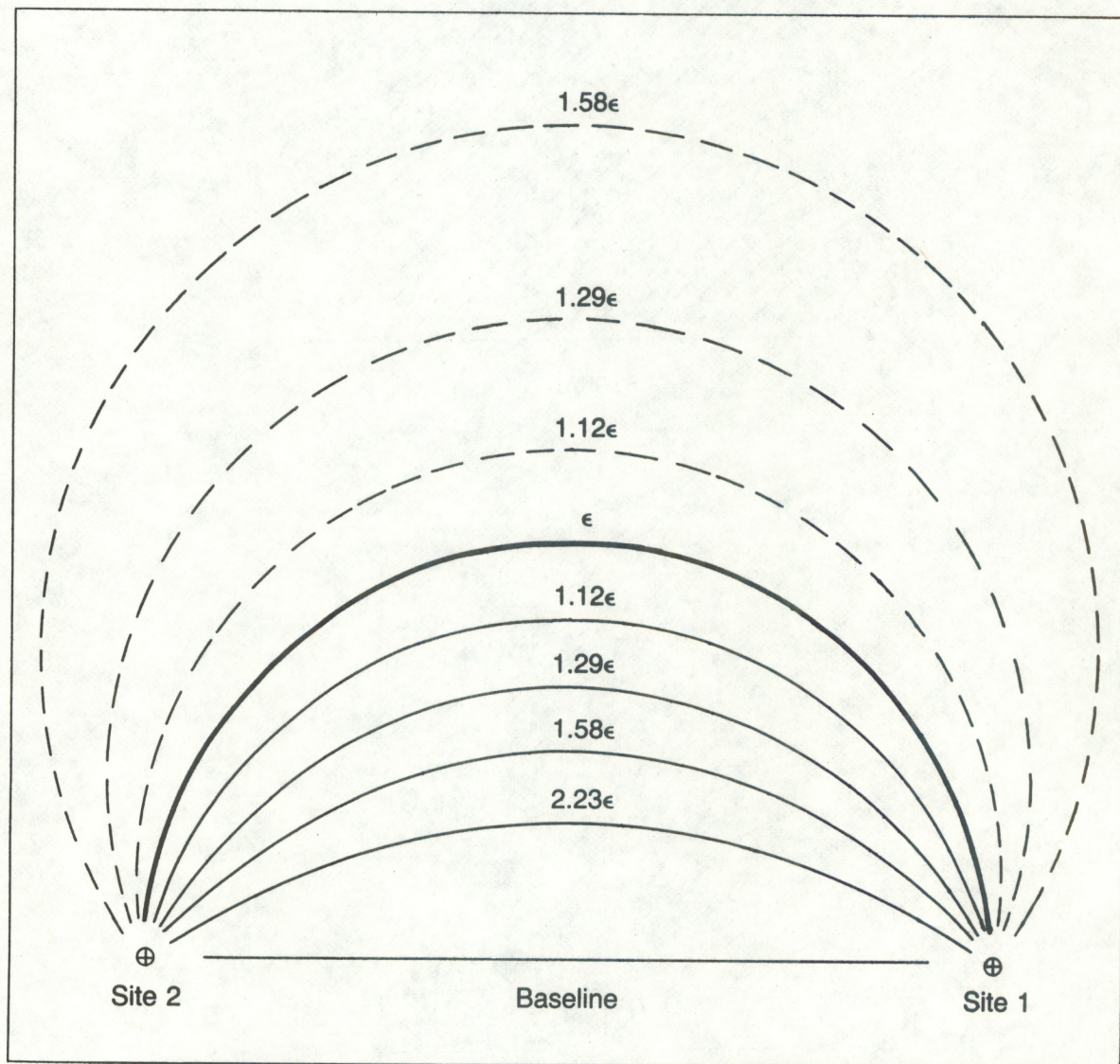
Figure 3.--Triangulation error curves obtained by incrementing $\cos(\gamma)$ in steps of ±0.2. These curves show how an error ϵ on the circle propagates with a deteriorating triangulation angle.

SIGNAL

DATA = SIGNAL + NOISE
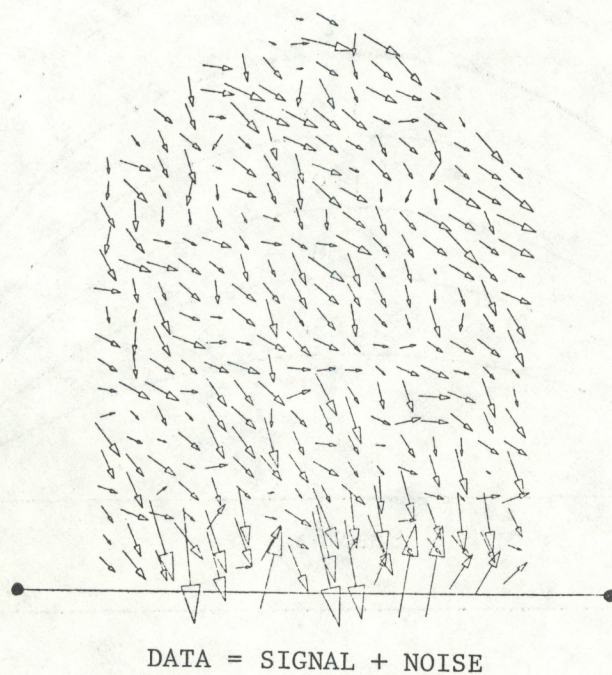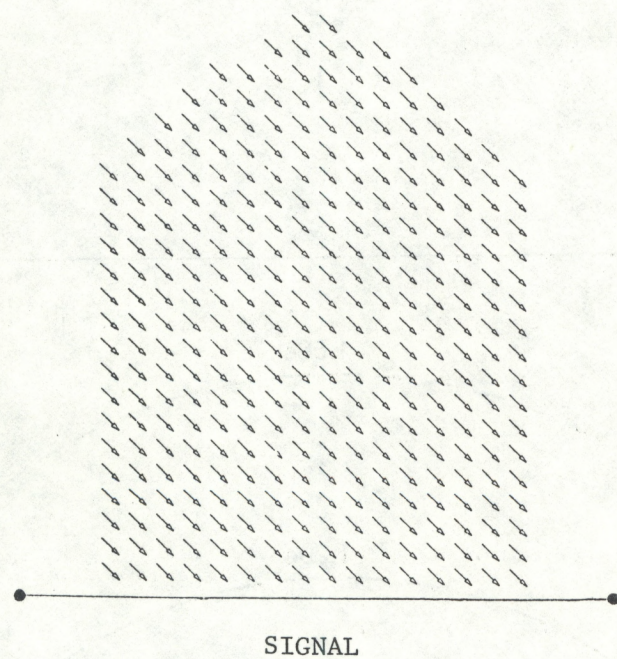
Figure 4.--Vector maps of a constant signal (upper) and noisy data (lower).

14

2.0ε

1.5ε

1.25ε
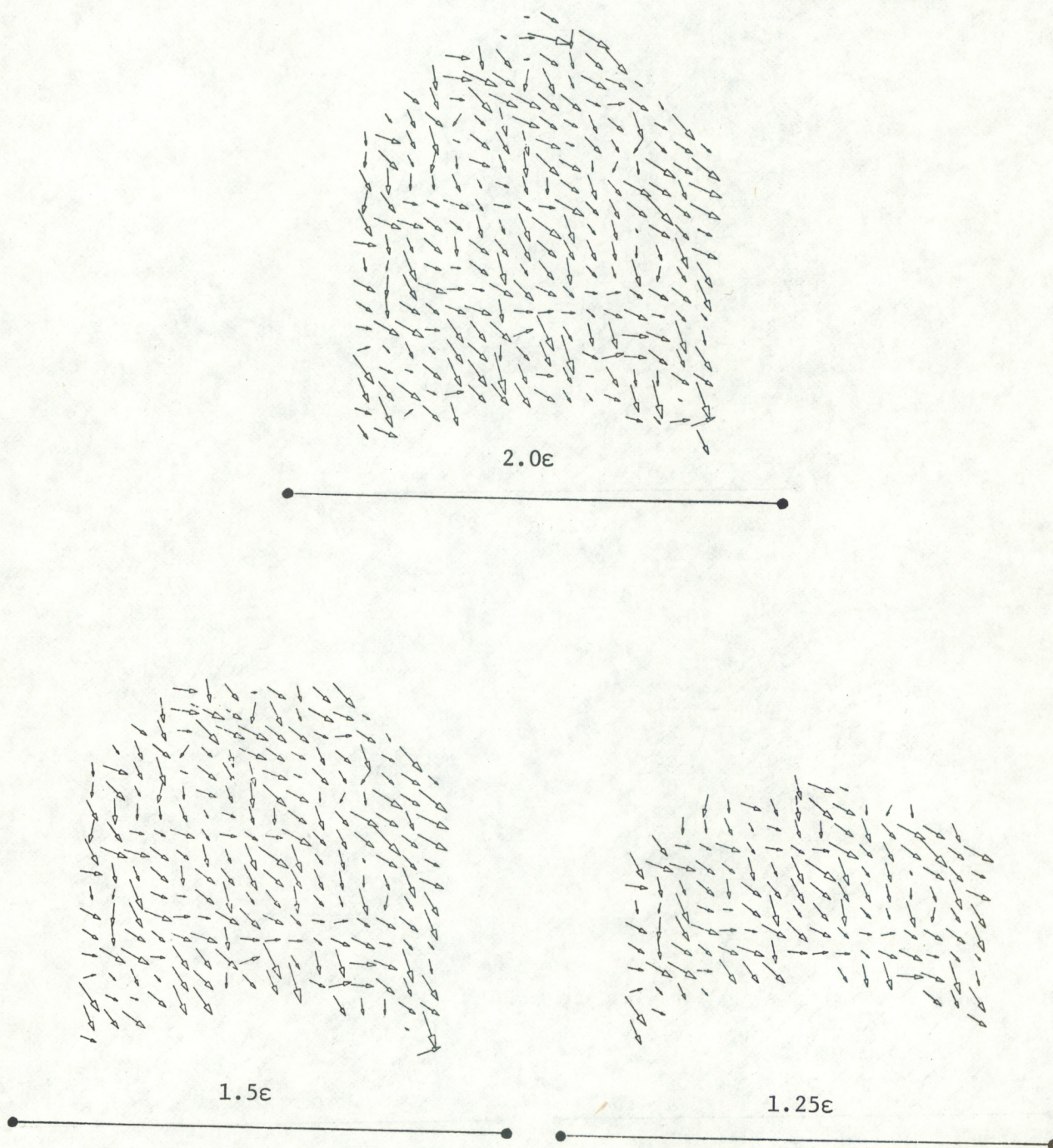
Figure 5.--The result of deleting the unstable regions for triangulation errors tε.
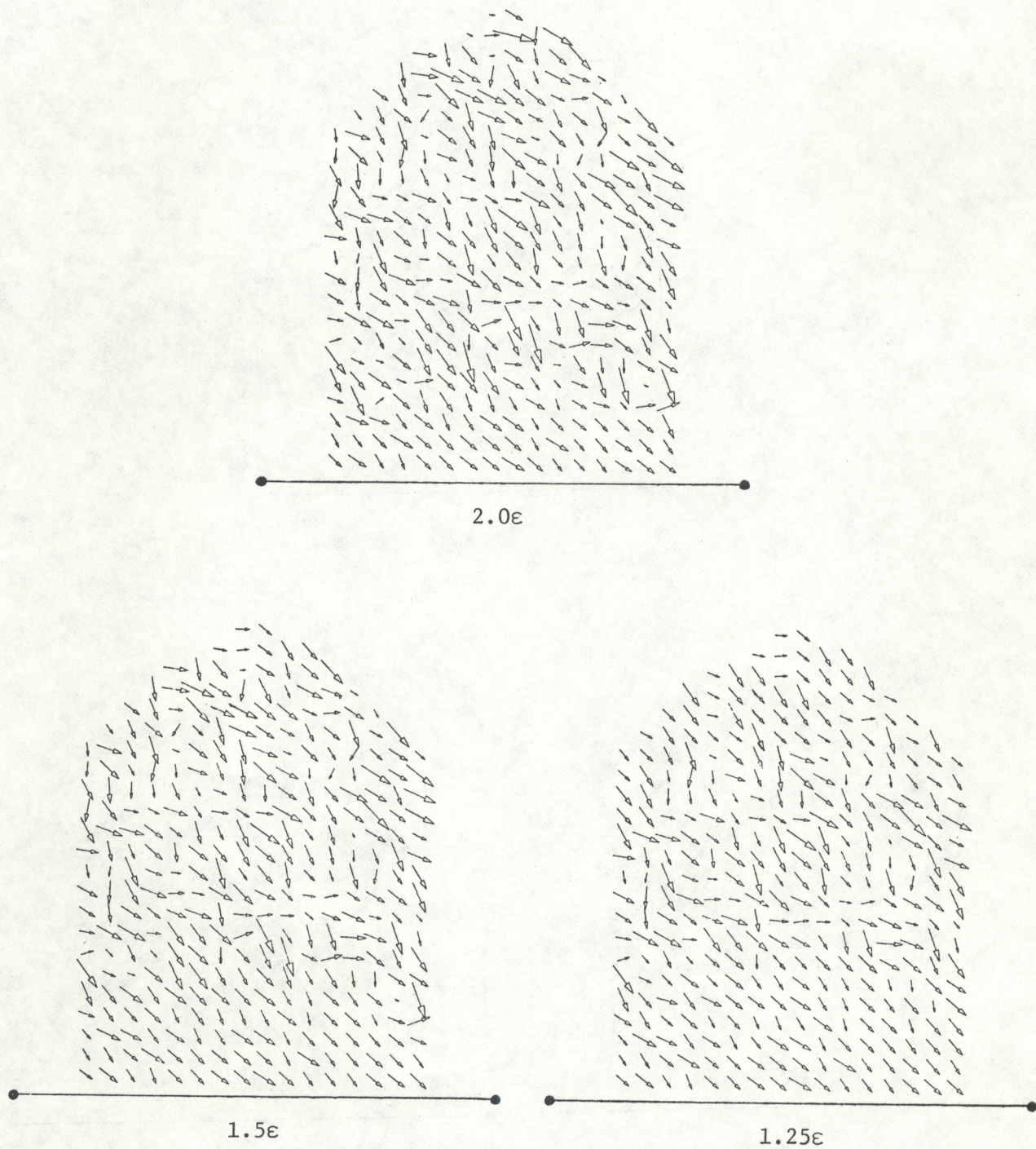
2.0ε

1.5ε

1.25ε
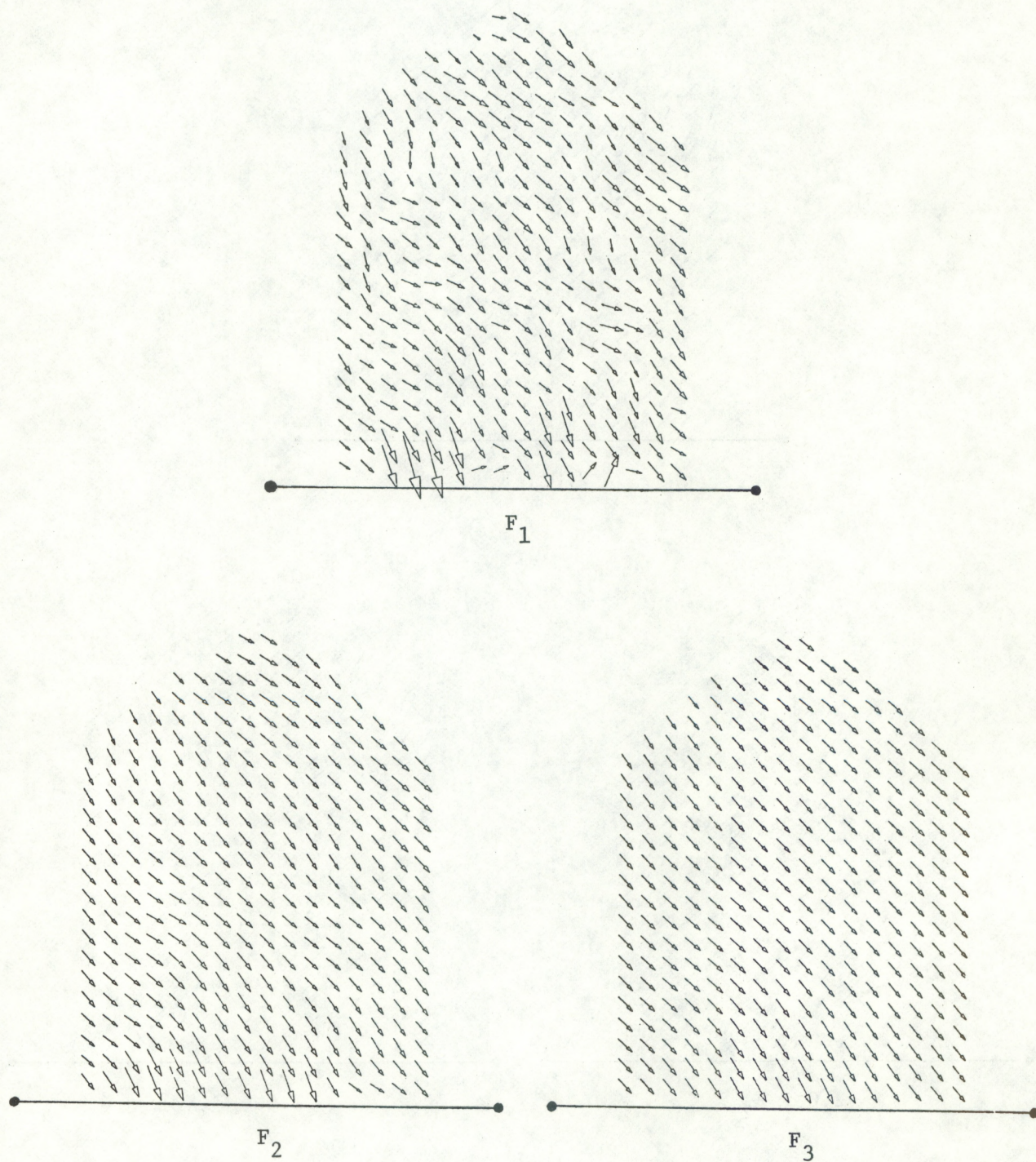
Figure 6.--Singular extension applied to the maps of Fig. 5.

Figure 7.--The result of applying low-pass filters F_1, F_2, and F_3 to noisy radial data used to get Fig. 4.
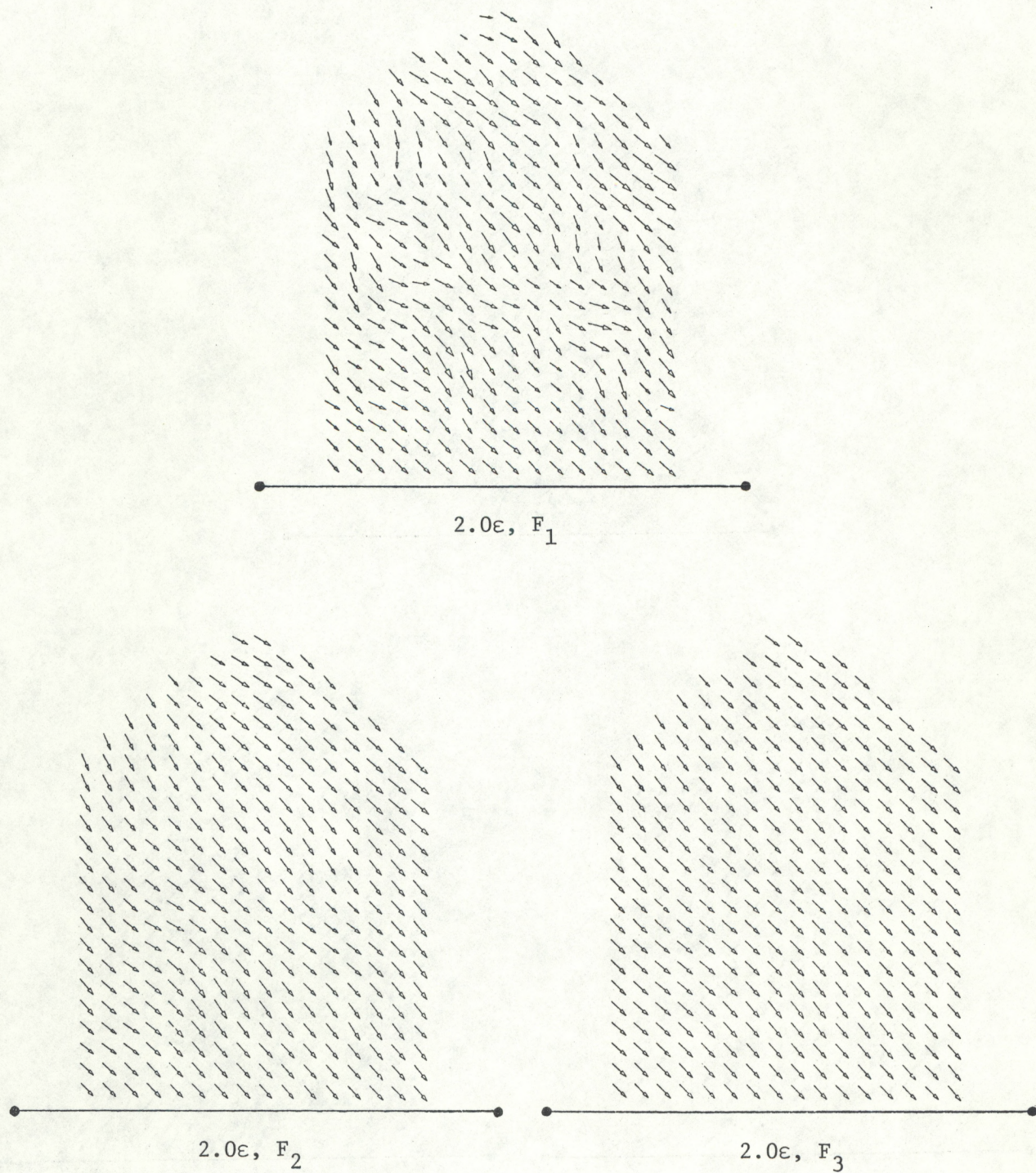
2.0ε, F₁

2.0ε, F₂

2.0ε, F₃

Figure 8.--The combined effect of filtering and singular extension. The filtering is the same as that of Fig. 7. The deleted region is the same as that in the upper map of Fig. 5.

18